
CHIMLE: Conditional Hierarchical IMLE for Multimodal Conditional Image Synthesis

Shichong Peng¹, Alireza Moazeni¹, Ke Li^{1,2}

¹APEX Lab

School of Computing Science
Simon Fraser University

²Google

{shichong_peng, seyed_alireza_moazenipourasil, keli}@sfu.ca

Abstract

A persistent challenge in conditional image synthesis has been to generate diverse output images from the same input image despite only one output image being observed per input image. GAN-based methods are prone to mode collapse, which leads to low diversity. To get around this, we leverage Implicit Maximum Likelihood Estimation (IMLE) which can overcome mode collapse fundamentally. IMLE uses the same generator as GANs but trains it with a different, non-adversarial objective which ensures each observed image has a generated sample nearby. Unfortunately, to generate high-fidelity images, prior IMLE-based methods require a large number of samples, which is expensive. In this paper, we propose a new method to get around this limitation, which we dub Conditional Hierarchical IMLE (CHIMLE), which can generate high-fidelity images without requiring many samples. We show CHIMLE significantly outperforms the prior best IMLE, GAN and diffusion-based methods in terms of image fidelity and mode coverage across four tasks, namely night-to-day, $16\times$ single image super-resolution, image colourization and image decompression. Quantitatively, our method improves Fréchet Inception Distance (FID) by 36.9% on average compared to the prior best IMLE-based method, and by 27.5% on average compared to the best non-IMLE-based general-purpose methods. More results and code are available on the project website at <https://niopeng.github.io/CHIMLE/>.

1 Introduction

Impressive advances in image synthesis have been made by generative models [9, 40, 83, 15, 78, 31, 38]. Generative models are probabilistic models; in the context of image synthesis, they aim to learn the probability distribution over natural images from examples of natural images. Whereas unconditional generative models learn the *marginal* distribution over images, conditional generative models learn the *conditional* distribution over images given a conditioning input, such as a class label, textual description or image.

Conditional generative modelling is more challenging than unconditional generative modelling, due to the need to ensure consistency between the conditioning input and the generated output while still ensuring image fidelity and diversity. As the conditioning input becomes more specific, there are fewer images in the training set that are consistent with the conditioning input, resulting in weaker supervision. So, in the order of decreasing supervision are class, text and image-conditional generative models – in class conditioning, many images correspond to each class; in text conditioning, multiple images can at times share the same textual description; in image conditioning (e.g., a grayscale image as the input and a colour image as the output), typically only one output image that corresponds to each input image is observed (e.g., only one way to colour a grayscale image is observed). We

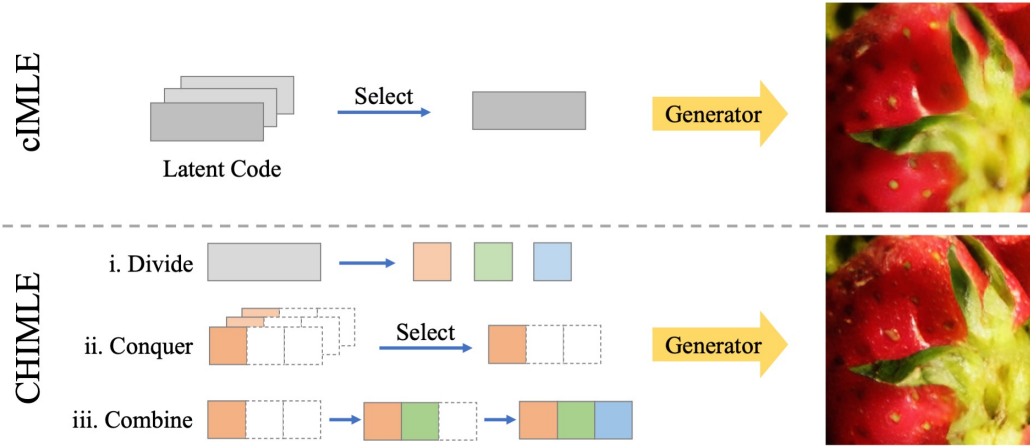


Figure 1: Overview of the prior best IMLE-based method, cIMLE [53] (top row) and the proposed method, CHIMLE (bottom row). Whereas cIMLE samples many latent codes and selects the one that produces the best result, CHIMLE divides the latent code by dimension into components, selects the best sample for each component and iteratively combines the selected components to form the overall latent code. As shown, the sample from CHIMLE contains more fine-grained details than the one from cIMLE.

will focus on the most challenging of these settings, namely image conditioning. Regardless of the supervision, the goal of conditional generative models is to learn the full distribution over all possible images consistent with the input.

Attaining this goal is challenging, especially when the supervision is weak, and so popular existing methods such as variational autoencoders (VAEs) [45, 70] and generative adversarial nets (GANs) [26, 27] focus on generating a point estimate of the conditional distribution, such as the mean (VAE) or an arbitrary mode (GAN). Such methods are known as *unimodal methods*, whereas methods that aim to generate samples from the full distribution are known as *multimodal methods*, since they enable samples to be drawn from as many modes as there exist.

Extending popular unconditional generative models such as VAEs, GANs and diffusion models to the image-conditional multimodal setting has proven to be challenging. VAEs suffer from posterior collapse [18, 57] where the encoder ignores the conditional input, leading the decoder to produce the conditional mean, which typically corresponds to a blurry image. GANs suffer from mode collapse [37, 105], where the generator tends to ignore the latent noise, leading the generator to produce the same mode of the conditional distribution for the same input regardless of the latent noise. As a result, other equally valid modes (e.g., other possible ways to colour a grayscale image) cannot be generated. Recent and concurrent work [42, 6] extends diffusion models to this setting, but they can produce both too little and too much diversity by creating spurious modes and dropping modes. We dub this problem *mode forcing* and include an analysis of its cause in the appendix.

A recent method [53] takes a different approach by extending an alternative generative modelling technique known as Implicit Maximum Likelihood Estimation (IMLE) [52] to the conditional synthesis setting. At a high level, IMLE uses a generator like GANs, but instead of using an adversarial objective which makes each generated sample similar to some *observed image*, IMLE uses a different objective that ensures each observed image has some similar *generated samples*. Hence, the generator can cover the whole data distribution without dropping modes. We refer interested readers to [53, 52] for more details on the algorithm.

However, as shown in the top row of Figure 1, the output image from cIMLE [53] lacks fine details. For cIMLE to generate high quality samples, there must a sample out of m samples generated during training that is similar to the observed image. This necessitates a large m ; unfortunately, generating a large number of samples is computationally expensive. So we are faced with a tradeoff: do improvements in sample quality have to come at the expense of sample efficiency?

In this paper, we show that there is a way around this conundrum. The idea is to generate samples in a clever way such that the best sample is about as similar to the observed image as if a large number of samples had been generated, *without* actually generating that many samples. We propose three ideas: partitioning of the latent code, partial evaluation of latent code components and iterative construction of latent code as shown in the bottom row of Figure 1. These three ideas give rise to a novel method known as Conditional Hierarchical IMLE (CHIMLE). We demonstrate that CHIMLE significantly outperforms the prior best IMLE-based method [53] in terms of both fidelity and diversity across four challenging tasks, namely night-to-day, $16\times$ single image super-resolution, image colourization and image decomposition. Moreover, we show that CHIMLE achieves the state-of-the-art results in image fidelity and mode coverage compared to leading general-purpose multimodal and task-specific methods, including both GAN-based and diffusion-based methods.

2 Method

2.1 Preliminaries: Conditional Implicit Maximum Likelihood Estimation (cIMLE)

In ordinary unimodal synthesis, the model is a function f_θ parameterized by θ that maps the input to the generated output. To support multimodal synthesis, one can add a latent random variable as an input, so now f_θ takes in both the input \mathbf{x} and a latent code \mathbf{z} drawn from a standard Gaussian $\mathcal{N}(0, \mathbf{I})$ and produces an image $\hat{\mathbf{y}}$ as output. To train such a network, we can use a conditional GAN (cGAN), which adds a discriminator network that tries to tell apart the observed image \mathbf{y} and the generated output $\hat{\mathbf{y}}$. The generator is trained to make its output $\hat{\mathbf{y}}$ seem as real as possible to the discriminator. Unfortunately, after training, $f_\theta(\mathbf{x}, \mathbf{z})$ often produces the same output for all values of \mathbf{z} because of mode collapse. Intuitively, this happens because making $\hat{\mathbf{y}}$ as real as possible would push it towards the observed image \mathbf{y} , so the generator tries to make its output similar to the observed image \mathbf{y} for all values of \mathbf{z} . As a result, naively applying cGANs to the problem of *multimodal* synthesis is difficult.

Conditional IMLE (cIMLE) [53] proposes an alternative technique for training the generator network f_θ . Rather than trying to make *all* outputs generated from different values of \mathbf{z} similar to the observed image \mathbf{y} , it only tries to make *some* of them similar to the observed image \mathbf{y} . The generator is therefore only encouraged to map one value of \mathbf{z} to the observed image \mathbf{y} , allowing other values of \mathbf{z} map to *other* reasonable outputs that are not observed. This makes it possible to perform *multimodal* synthesis. Also, unlike cGANs, cIMLE does not use a discriminator and therefore obviates adversarial training, making training more stable. The cIMLE training objective is:

$$\min_{\theta} \mathbb{E}_{\mathbf{z}^{(1,1)}, \dots, \mathbf{z}^{(n,m)} \sim \mathcal{N}(0, \mathbf{I})} \left[\sum_{i=1}^n \min_{j \in \{1, \dots, m\}} d(f_\theta(\mathbf{x}^{(i)}, \mathbf{z}^{(i,j)}), \mathbf{y}^{(i)}) \right], \quad (1)$$

where $d(\cdot, \cdot)$ is a distance metric, m is a hyperparameter, and $\mathbf{x}^{(i)}$ and $\mathbf{y}^{(i)}$ are the i^{th} input and observed image in the dataset. During each iteration of the training loop, a *pool* of m samples are generated from f_θ for each input $\mathbf{x}^{(i)}$. The cIMLE algorithm then selects the *closest* sample for each observed image $\mathbf{y}^{(i)}$ to optimize θ .

2.2 Conditional Hierarchical IMLE (CHIMLE)

In order to generate high-quality images using cIMLE, we need some of the m generated samples to be similar to the observed image \mathbf{y} during training. Achieving this requires a large m , but generating samples is expensive. This forces a tradeoff between the number of samples and the mode modelling accuracy, which is less than ideal.

The key observation is that the gradient of the loss depends solely on the *closest* sample for each observed image, as shown in Eqn. 1 – all other samples that are not selected do not contribute. Therefore, if we could efficiently search for a latent code \mathbf{z} that would produce a sample of a comparable degree of similarity to \mathbf{y} as one that would be selected from a larger pool \mathbf{z}^* , we could achieve high sample quality without actually generating that many samples.

To solve search problems, a time-tested paradigm in computer science is divide-and-conquer, which entails *dividing* the problem into simpler sub-problems, *conquering* each sub-problem and *combining* the solutions from the solved sub-problem. In the context of searching for a latent code \mathbf{z} that

simulates the quality of \mathbf{z}^* , we propose dividing the latent code into components, evaluating each latent code component and combining the latent code components iteratively.

In the ensuing discussion, we will consider a common paradigm of image synthesis models [68, 37, 13, 39], where the model processes the image at L different scales. We can feed different dimensions of the latent code as inputs to different layers operating at different resolutions, thereby controlling the variations of content at different resolutions.

Division of Latent Code To reduce the difficulty of the original problem, we can divide it into sub-problems. Each of these sub-problems should be a simpler instance of the original problem. We propose dividing the dimensions of the latent code $\mathbf{z} \in \mathbb{R}^n$ into L different components $S = \{\mathbf{z}_i\}_{i=1}^L$, where $\mathbf{z}_i \in \mathbb{R}^{k_i}$ and $\sum_{i=1}^L k_i = n$, which amounts to dividing the latent space into mutually orthogonal subspaces. Each component \mathbf{z}_i corresponds to the dimensions that serve as input to layers operating at a particular resolution.

Partial Evaluation of Latent Code Components To determine how promising a latent code component is, we need a way to evaluate a partially constructed latent code, with only some components, indexed by $S_r \subset S$, being realized with concrete values. We propose using a partial output $\tilde{\mathbf{y}}_p$ that depends only on the currently constructed components \mathbf{z}_{S_r} , and evaluating $\tilde{\mathbf{y}}_p$ against a part of the observed image \mathbf{y}_p that only contains details at resolutions modelled by \mathbf{z}_{S_r} . So instead of computing $d(\tilde{\mathbf{y}}, \mathbf{y})$, we compute $d(\tilde{\mathbf{y}}_p, \mathbf{y}_p)$. By doing so, we can evaluate the quality of \mathbf{z}_{S_r} more accurately, since $\tilde{\mathbf{y}}_p$ does not depend on the unconstructed components $\mathbf{z}_{S \setminus S_r}$. To realize this, we add output heads at the L different resolutions that the model operates on to produce the partial outputs $\tilde{\mathbf{y}}_p$ and downsample the observed image \mathbf{y} to the corresponding resolutions to produce the partial observed images \mathbf{y}_p . The values of the partially realized components that result in the greatest similarity to \mathbf{y}_p is the final selected component, i.e., $\mathbf{z}_p^* = \arg \min d(\tilde{\mathbf{y}}_p, \mathbf{y}_p)$.

Algorithm 1 Conditional Hierarchical IMLE Algorithm for a Single Data Point

Require: One input image at L increasing resolutions $\{\mathbf{x}_l\}_{l=1}^L$, the set of partial observed images $\{\mathbf{y}_l\}_{l=1}^L$ at corresponding resolutions and the generator $f_\theta(\cdot, \cdot)$ that produces L outputs at corresponding resolutions

for $l = 1$ **to** L **do**

Randomly generate m i.i.d. latent codes for the l^{th} component $\mathbf{z}_l^{(1)}, \dots, \mathbf{z}_l^{(m)}$

$\tilde{\mathbf{y}}_l^{(j)} \leftarrow l^{\text{th}}$ output from

$f_\theta((\mathbf{x}_1, \dots, \mathbf{x}_l), (\mathbf{z}_1^*, \dots, \mathbf{z}_{l-1}^*, \mathbf{z}_l^{(j)})) \forall j \in \{1, \dots, m\}$

$\mathbf{z}_l^* \leftarrow \arg \min_j d(\mathbf{y}_l, \tilde{\mathbf{y}}_l^{(j)}) \forall j \in \{1, \dots, m\}$

end for

return $\{\mathbf{z}_l^*\}_{l=1}^L$

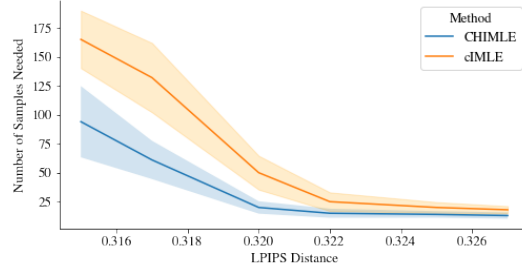


Figure 2: Generated sample quality comparison between the proposed Conditional Hierarchical IMLE (CHIMLE) and cIMLE [53]. The plot shows the number of generated samples needed to reach the same distance (as measured by LPIPS) to the observed image with CHIMLE or cIMLE. A smaller number of generated samples means better efficiency in finding a sample that is close to the observed image. The result is averaged over ten independent runs. As shown, CHIMLE consistently outperforms cIMLE by requiring significantly fewer samples. Also, the more stringent the required LPIPS distance gets, the greater the disparity between the number of samples needed by cIMLE vs. CHIMLE.

Iterative Combination of Latent Code Components To maximize efficiency, the solution to one sub-problem should reveal some information on which other sub-problems to solve. So, we need to decide on which sub-problems to solve first and how to use their solutions to decide on which sub-problem to solve next. We leverage the fact that solving for the appearance at lower resolutions (e.g., finding out that the coarse structure of an apple is red) can inform on the probable appearances

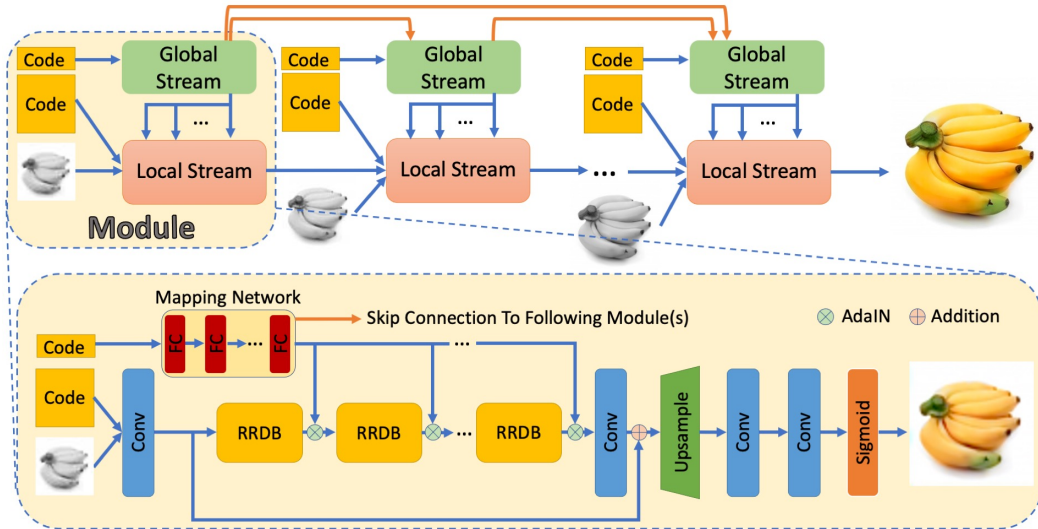


Figure 3: Our model consists of multiple modules, each of which operates on $2\times$ the resolution of the previous one. Each module contains a global stream and a local stream. The local stream consists of a sequence of residual-in-residual dense blocks (RRDB). The global stream consists of a mapping network which applies adaptive instance normalization (AdaIN) to the output of each RRDB block.

at higher resolutions (e.g., the fine details of the apple are likely red as well). We propose starting the construction of the latent code from the component operating at the lowest resolution to the highest, i.e. from \mathbf{z}_1 to \mathbf{z}_L , where \mathbf{z}_i 's are assumed to be ordered by resolution in increasing order. At a given resolution $l \in \{1 \dots L\}$, we set the components at all lower resolutions to the values selected in previous steps $\mathbf{z}_1^*, \dots, \mathbf{z}_{l-1}^*$ to construct $\mathbf{z}_{S_l} = (\mathbf{z}_1^*, \dots, \mathbf{z}_{l-1}^*, \mathbf{z}_l)$, and evaluate the quality of \mathbf{z}_{S_l} using the partial evaluation method proposed above.

Putting everything together, we obtain the Conditional Hierarchical IMLE (CHIMLE) algorithm, which is detailed in Alg. 1 for the special case of one input image. We validate the effectiveness of CHIMLE by comparing the number of generated samples CHIMLE needs to obtain the same level of similarity to the observed image as cIMLE. As shown in Figure 2, CHIMLE consistently requires fewer samples than cIMLE, demonstrating a significant improvement in sample efficiency.

2.3 Model Architecture

As shown in Figure 3, our architecture contains a sequence of modules, each of which handles an input image of a particular resolution and outputs an image whose resolution is doubled along each side. We downsample the input image repeatedly by half to obtain input images at different resolutions, which are fed into different modules. As mentioned in Sect. 2.2, we divide the dimensions of the latent code into components and feed each to a different module. Note that this architecture generalizes to varying levels of output resolution, since we can simply add more modules for high-resolution outputs. We add intermediate output heads to each module and add supervision to the output of each module. We choose LPIPS [101] as the distance metric used in the IMLE objective function.

For the design of each module, we follow the paradigm of prior work on modelling global and local image features [59, 10, 84, 58, 74] and design a module that comprises of two branches, a local processing branch and a global processing branch. The local processing branch takes in the conditional image input, a latent code with the matching resolution as the image and the output from the previous module if applicable. The global processing branch takes in a fixed-sized latent code input and produces scaling factors and offsets for the different channels of the intermediate features in the local processing branch. For more implementation details, please refer to the appendix. Due to the hierarchical nature of the architecture and its role as the implicit model in IMLE (also known as the “generator” in GAN parlance), we dub this architecture the Tower Implicit Model (TIM).

3 Experiments

Baselines To validate our main contribution of this paper, namely improving the output fidelity of IMLE-based methods, we compare to the leading IMLE-based method, cIMLE [53]. As a

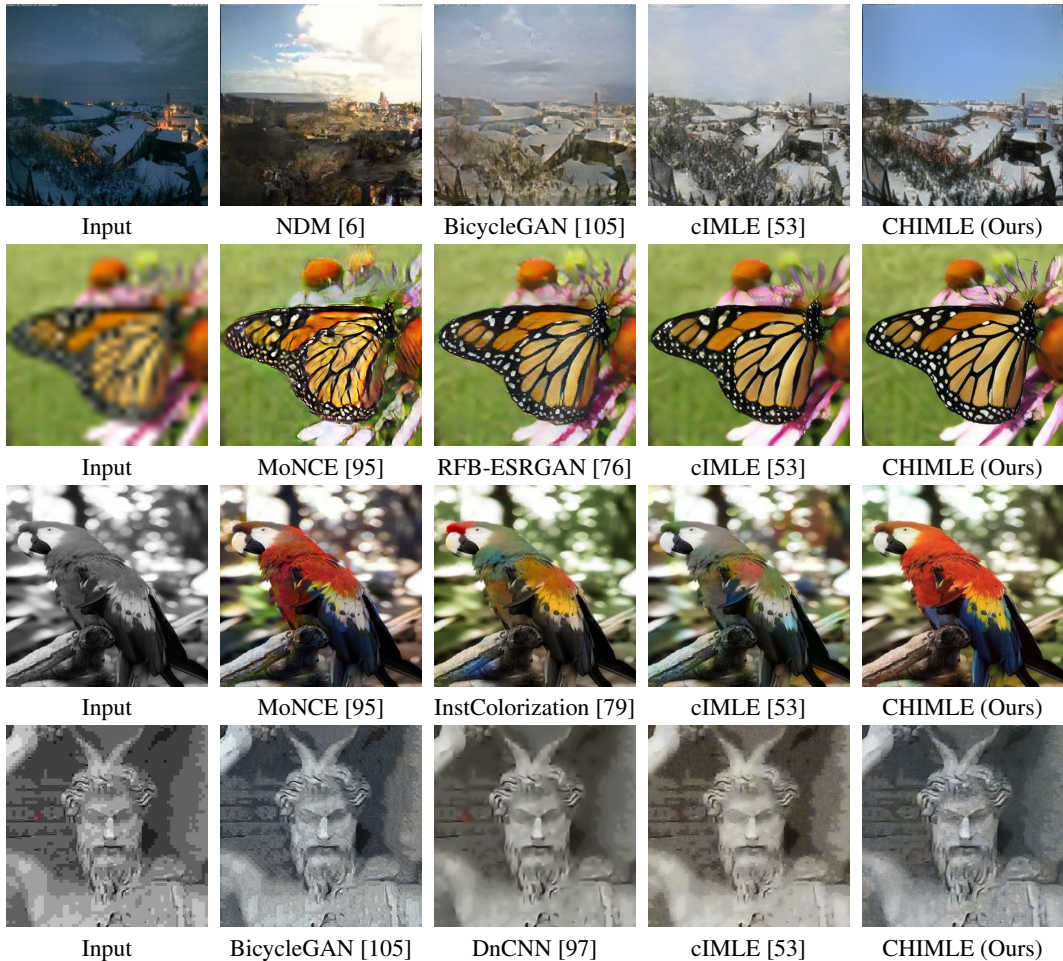


Figure 4: Qualitative comparison of our method (CHIMLE) and selected baselines on night-to-day (1st row), 16 \times super-resolution (2nd row), image colourization (3rd row) and image decompression (4th row). In each row, we show the results from the best performing general-purpose baseline, a strong task-specific baseline (if applicable), the best prior IMLE-based method cIMLE [53] and CHIMLE. Better viewed zoomed-in. As shown, CHIMLE correctly preserves the details of the input while generating fine-grained details in the output, which compares favourably to the baselines.

secondary comparison, we demonstrate potential impact in a broader context and compare our method to the leading multimodal general-purpose conditional image synthesis methods according to a recent survey [65], including four GAN-based methods, such as BicycleGAN [105], MSGAN [60], DivCo [56] and MoNCE [95], and two diffusion-based methods, such as DDRM [42] and NDM [6]. As a tertiary comparison, we also compare our method to popular task-specific methods based on leaderboard rankings in challenges and recent survey papers [96, 3].

Tasks We apply our method to four different conditional image synthesis tasks, namely night-to-day, 16 \times single image super-resolution, image colourization and image decompression. We pick night-to-day because it is a classic task in the multimodal general-purpose conditional image synthesis literature [37, 105]. We pick the remaining tasks because they are more challenging than typical tasks considered in the literature as evidenced by the availability of task-specific methods tailored to each.

Training Details We use a four-module TIM model (described in Sect. 2.3) for all tasks. The input to each module is downsampled from the full resolution input to resolution the module operates on. We trained all models for 150 epochs with a mini-batch size of 1 using the Adam optimizer [44] on an NVIDIA V100 GPU. Details for datasets are included in the appendix.

Evaluation Metrics We evaluate the visual fidelity of generated output images using the Fréchet Inception Distance (FID) [30] and Kernel Inception Distance (KID) [7]. We also measure the diversity of the generated output images since it is a crucial objective of *multimodal* conditional image

synthesis. One metric to measure diversity is the LPIPS diversity score (not to be confused with the LPIPS distance metric) [105], which is the average LPIPS distance between different output samples for the same input. Unfortunately it has limitations, because it may favour a set of samples where some are of poor fidelity as shown in Figure 5. To get around this, we use faithfulness-weighted variance (FwV) [53] instead, which is the average LPIPS distance d_{LPIPS} between the output samples and the mean, weighted by the consistency with the original image measured by a Gaussian kernel ¹:

$$\mathcal{M} = \sum_i \sum_j w_i d_{\text{LPIPS}}(\tilde{\mathbf{y}}^{(i,j)}, \bar{\mathbf{y}}^{(j)}), \text{ where } w_i = \exp\left(\frac{-d_{\text{LPIPS}}(\tilde{\mathbf{y}}^{(i,j)}, \mathbf{y}^{(j)})}{2\sigma^2}\right) \quad (2)$$

where $\tilde{\mathbf{y}}^{(i,j)}$ is the i^{th} generated sample from the j^{th} input. $\bar{\mathbf{y}}^{(j)}$ is the mean of all generated samples from the j^{th} input. $\mathbf{y}^{(j)}$ is the j^{th} observed image. The kernel bandwidth parameter σ trades off the importance of consistency vs. diversity.



	LPIPS Diversity \uparrow	Faithfulness-weighted Variance ($\sigma=0.2$) \uparrow	Samples
Group 1	0.079	0.0045	
Group 2	0.217	0.0034	

Figure 5: Comparisons of LPIPS diversity score and faithfulness-weighted variance on two groups of sample images. Although Group 2 achieves a better LPIPS diversity score (shown on the left), some of the samples have poor visual fidelity. Group 1 contains samples that are both diverse (zoom in for difference in the seeds on the surface of the strawberry) and of high visual fidelity, which is preferred by the faithfulness-weighted variance (shown on the left).

We measure how well the modes in the model distribution and the true distribution match along two axes, mode accuracy (precision) and mode coverage (recall). We measure the former with the $F_{1/8}$ score component of the PRD metric [71], which is heavily weighted towards precision, and the latter with the F_8 score component of the PRD metric [71], which is heavily weighted towards recall, and the inference-via-optimization (IvO) metric [61], which measures the final mean squared error (MSE) between the the observed image and the best output image that can be generated (i.e., where the latent code is optimized w.r.t. MSE while keeping model weights fixed). In the conditional image synthesis setting, IvO is a more sensitive metric than the F_8 score in PRD, since it would detect cases where the output samples for a given input are not diverse but the output samples for different inputs are diverse in aggregate. In other words, IvO measures mode coverage in the conditional distribution, whereas the F_8 score measures mode coverage in the marginal distribution. In light of the large number of noise samples in NDM (2 for each of the 1000 diffusion steps) which all need to be optimized in calculating IvO, we omit it due to the lack of sufficient computational resources.

3.1 Quantitative Results

We compare the perceptual quality and output diversity in Table 1. As shown, CHIMLE outperforms best prior IMLE-based method, cIMLE, general-purpose conditional image synthesis methods and task-specific methods in terms of FID and KID across all tasks. CHIMLE also outperforms all multimodal baselines in terms of FwV across all tasks. These results show that CHIMLE can produce more realistic and diverse images than the baselines, thereby setting a new state-of-the-art.

We compare the mode accuracy and coverage in Table 2. As shown, CHIMLE outperforms or achieves comparable performance to cIMLE and other multimodal general-purpose baselines in

¹ $\exp(-d_{\text{LPIPS}}(\cdot, \cdot)/2\sigma^2)$ is considered a Gaussian kernel rather than a Laplacian kernel because LPIPS distance is defined as a *squared* Euclidean distance in feature space.

	Night-to-day			Super-Resolution (SR)			Colourization (Col)			Image Decompression (DC)		
	FID ↓	KID ↓	FwV ↑	FID ↓	KID ↓	FwV ↑	FID ↓	KID ↓	FwV ↑	FID ↓	KID ↓	FwV ↑
General-Purpose Methods:												
<i>GAN-based:</i>												
<i>BicycleGAN [105]</i>	179.08	132.35	0.23	67.17	53.28	0.84	53.33	34.44	7.44	<u>87.35</u>	<u>20.24</u>	0.29
<i>MSGAN [60]</i>	213.81	176.55	0.18	83.65	67.47	0.76	53.53	31.12	10.23	100.58	27.75	0.31
<i>DivCo [56]</i>	179.85	136.47	0.22	66.97	54.86	0.65	53.82	34.44	12.49	92.76	24.44	0.25
<i>MoNCE [95]</i>	232.10	217.79	0.18	47.97	35.31	0.68	27.67	9.55	<u>18.30</u>	113.21	27.56	1.12
<i>Diffusion-based:</i>												
<i>DDRM [42]</i>	324.01	258.69	0.04	178.62	170.72	0.80	138.88	121.77	3.06	157.00	61.08	0.68
<i>NDM [6]</i>	167.50	132.93	0.28	118.30	106.51	1.84	43.98	16.21	14.39	136.32	52.64	0.67
Task-Specific Methods:												
<i>RFB-ESRGAN (SR) [76]</i>	–	–	–	<u>19.90</u>	<u>8.01</u>	–	–	–	–	–	–	–
<i>InstColorization (Col) [79]</i>	–	–	–	–	–	–	<u>26.37</u>	<u>8.52</u>	–	–	–	–
<i>DnCNN (DC) [97]</i>	–	–	–	–	–	–	–	–	–	109.38	48.05	–
IMLE-based Methods:												
<i>cIMLE [53]</i>	<u>166.28</u>	<u>123.15</u>	<u>0.47</u>	28.42	14.75	<u>5.22</u>	63.00	49.30	14.65	101.66	30.11	<u>3.14</u>
<i>CHIMLE (Ours)</i>	141.44	90.10	0.51	16.01	4.54	5.61	24.33	7.73	27.11	73.69	12.12	3.80

Table 1: Comparison of fidelity of generated images, measured by the Fréchet Inception Distance (FID) and Kernel Inception Distance (KID), and diversity, measured by faithfulness-weighted variance (FwV). We show the results by our method (CHIMLE) and the leading IMLE-based, task-specific baselines and general-purpose conditional image synthesis baselines. Lower values of FID/KID are better and a higher value of faithfulness-weighted variance shows more variation in the generated samples that are faithful to the observed image. For FwV, we show the results for the bandwidth parameter $\sigma = 0.2$ as it achieves a good balance between consistency and diversity. The KID and the FwV are shown on the scale of 10^{-3} . “–” indicates metric not applicable. We compare favourably relative to the baselines.

terms of PRD scores. In addition, CHIMLE significantly outperforms cIMLE and other multimodal general-purpose baselines in terms of IvO. These results show that CHIMLE achieves better mode accuracy and coverage of the true distribution compared to the baselines.

3.2 Qualitative Results

We show the qualitative comparison of our method (CHIMLE) and selected baselines on various tasks in Figure 4. As shown, CHIMLE generates high-quality results, like the high contrasts in the building and the bushes in night-to-day (1st row), the sharp appearance of the wing pattern of the butterfly wing and the flowers in the background (2nd row), the vibrant yet detailed colouring of the parrot (3rd row) and the high-frequency details in the sculpture (4th row). For all methods, we show videos of different samples generated from the same input on the project website and in the supplementary materials. Due to mode collapse, GAN-based baselines incorporate regularizers that improve the diversity of samples at the expense of their fidelity, resulting in more varied but less realistic samples as shown in the videos. Diffusion-based baselines suffer from *mode forcing* (see appendix D for more details) and generate spurious samples that are either excessively diverse or with little diversity. The prior best IMLE-based method (cIMLE) avoids spurious samples but falls short in image fidelity. In contrast, CHIMLE generates samples that are both diverse and of high fidelity. Figure 6 shows the qualitative comparison of the best reconstruction of the observed image found by different methods using IvO [61], which tries to approximately invert each model by optimizing over the latent code input to find a generated image closest to the observed image. As shown, the reconstruction of the CHIMLE model is the closest to the observed image and achieves almost pixel-level accuracy. In addition, we found that for our model, IvO can consistently converge to a high-quality sample, whereas it would diverge quite often for the baselines, suggesting that inverting our model is much easier than the baselines. This demonstrates that CHIMLE successfully covers the mode corresponding to the observed image.

3.3 Ablation Study

We incrementally remove (1) iterative combination (IC), (2) partial evaluation (PE), (3) latent code division (CD). As shown in Figure 7, each is critical to achieving the best results. Notably, we see an average increase in terms of FID by 7.7% after removing IC, by another 7.8% after removing PE and by another 12.8% after removing CD, thereby validating the importance of each of our contributions.

	Night-to-day			Super-Resolution (SR)			Colourization (Col)			Image Decompression (DC)		
	PRD \uparrow		$IvO \downarrow$	PRD \uparrow		$IvO \downarrow$	PRD \uparrow		$IvO \downarrow$	PRD \uparrow		$IvO \downarrow$
	F_8 (Recall)	$F_{1/8}$ (Precision)		F_8 (Recall)	$F_{1/8}$ (Precision)		F_8 (Recall)	$F_{1/8}$ (Precision)		F_8 (Recall)	$F_{1/8}$ (Precision)	
<i>GAN-based:</i>												
BicycleGAN [105]	0.95	0.59	61.10 \pm 0.23	0.90	0.39	15.26 \pm 0.38	0.94	0.63	11.85 \pm 1.78	0.94	0.71	9.70 \pm 2.93
MSGAN [60]	0.96	0.50	86.3 \pm 2.03	0.92	0.42	16.51 \pm 0.64	0.93	0.62	11.60 \pm 2.07	0.95	0.74	8.00 \pm 1.10
DivCo [56]	0.94	0.46	59.50 \pm 0.91	0.87	0.33	13.82 \pm 0.32	0.92	0.61	10.88 \pm 1.20	0.93	0.68	6.38 \pm 1.08
MoNCE [95]	0.94	0.43	19.40 \pm 0.01	0.85	0.35	56.23 \pm 0.71	<u>0.95</u>	0.75	13.10 \pm 0.79	0.92	<u>0.76</u>	23.50 \pm 0.10
<i>Diffusion-based:</i>												
DDRM [42]	0.38	0.12	134.00 \pm 0.24	0.73	0.18	11.81 \pm 0.05	0.80	0.44	13.70 \pm 0.51	0.89	0.57	5.44 \pm 0.01
NDM [6]	0.90	0.56	–	0.78	0.19	–	0.97	<u>0.84</u>	–	0.81	0.51	–
<i>IMLE-based:</i>												
cIMLE [53]	<u>0.96</u>	<u>0.58</u>	1.54 \pm 1.04	0.86	0.32	6.78 \pm 0.43	0.92	0.64	0.71 \pm 0.09	0.91	0.74	5.86 \pm 0.20
CHIMLE (Ours)	0.97	0.58	0.96 \pm 0.04	0.96	0.78	1.49 \pm 0.11	0.97	0.87	0.32 \pm 0.01	0.95	0.83	0.31 \pm 0.10

Table 2: Comparison of mode accuracy, measured by $F_{1/8}$ score of the PRD metric [71], and mode coverage, measured by F_8 score of the PRD metric [71] and the inference-via-optimization metric (IvO) [61], between the model distribution and the true distribution by our method (CHIMLE) and the leading IMLE-based and general-purpose conditional image synthesis baselines. A higher value of the F_8 score shows better mode coverage (recall) and a higher value of the $F_{1/8}$ shows better mode accuracy (precision). A lower value of IvO shows better mode coverage since it indicate that the model can generate samples close to the observed images. For IvO, we show the average result across 5 independent runs on the scale of 10^{-3} . As shown, CHIMLE outperforms or achieves comparable performance to the baselines.

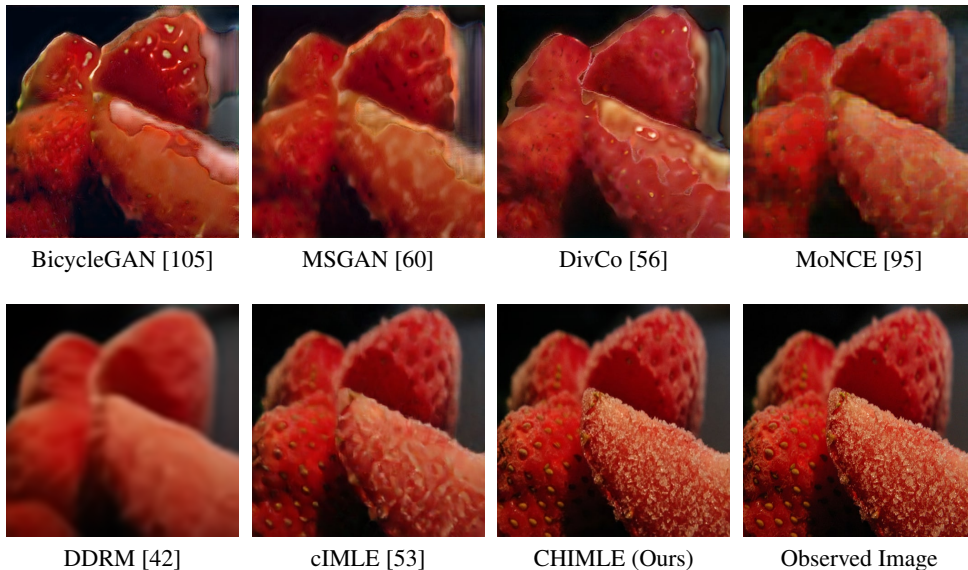


Figure 6: Qualitative comparison of best reconstructions of the observed image found by optimizing over the latent code input using the method of Inference via Optimization (IvO) [61]. The optimization starts by feeding a random latent code input to each method and minimizes the reconstruction loss from the model output to the observed image by optimizing the latent code input. As shown, the CHIMLE model allows for significantly better reconstruction of the observed image than the other methods, which demonstrates that the mode corresponding to the observed image is successfully covered by CHIMLE.

4 Related Work

General-Purpose Conditional Image Synthesis Conditional image synthesis generate images from a conditioning input. The input can come in various forms, such as a class label [62, 64], a textual description [69], or an image [37]. The latter is sometimes known as image-to-image translation, which is the setting we consider. General image-conditional methods can be paired or unpaired. In the paired setting, each image in the source domain corresponds to an image in the target domain [37, 93, 86, 75]. In the unpaired setting, images in the source domain may not correspond to images in the target domain [104, 92, 81, 55, 16, 8, 67]. Whereas these previous methods are all unimodal, other methods aim for the more challenging task of multimodal synthesis in the paired setting [105, 24, 22] and in the unpaired setting [34, 50, 51, 17]. Since many of the aforementioned works use GANs as their generators which suffer from mode collapse, some works aim to address this issue by introducing mode seeking terms [60] or adding contrastive losses [56, 95, 33]. Another

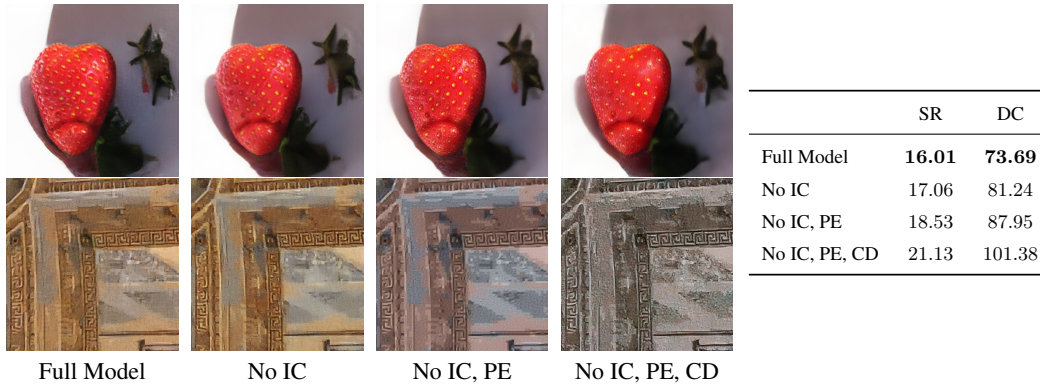


Figure 7: Qualitative (left figure) and quantitative (right table) of Fréchet Inception Distance (FID) comparison as we gradually remove (1) iterative combination (IC), (2) partial evaluation (PE), (3) latent code division (CD) on two tasks, $16\times$ super-resolution (SR) (first row in the figure) and image decompression (DC) (second row in the figure). As shown in the figure, the generated image contains less fine details (as in SR, where the strawberry seeds become less pronounced) or colour saturation (as in DC) as we remove each component, which is also reflected by the FID shown in the table.

line of work uses diffusion models [42, 6]. These methods can both generate spurious modes and drop modes (due to the problem of *mode forcing*, which we analyze in appendix D), and need to devote part of the model capacity to reconstruct the information encoded in the conditioning input from pure noise and retain it over the course of diffusion. In this paper, we focus on the paired image-conditional multimodal setting, and sidestep mode collapse by building on a recent generative modelling technique, conditional IMLE [53].

Task-Specific Approaches There is a large body of work on super-resolution, most of which consider upscaling factors of $2 - 4\times$. See [91, 63, 89] for comprehensive surveys. Many methods regress to the high-resolution image directly and differ widely in the architecture [23, 43, 47, 80, 28, 102, 19, 54]. Various conditional GANs have also been developed for the problem [49, 72, 88, 94, 66, 90, 87, 76]. For image colourization, a recent survey [3] provides a detailed overview of different methods. Some methods [14, 12, 100, 11] use deep networks to directly predict the colour and combine it with the input to produce the output. Other methods [36, 48, 21, 103, 79] take advantage of features from different levels or branches in the network for colour prediction. There is relatively little work on image decompression to our knowledge. [4] targets DCT-based compression methods and explicitly models the quantization errors of DCT coefficients. More work was done on learned image compression [2, 1], which changes the encoding of the compressed image itself. Another related area is image denoising, see [82] for a survey of deep learning methods. Many of the methods uses a ResNet [29] backbone or other variants of deep CNNs [97–99, 85].

5 Discussion and Conclusion

Limitation Our method can only generate output images that are similar to some training images. Take colourization as an example – if there were no green apple in the training data, then our model would not be able to generate green apples.

Societal Impact The TIM architecture adopts a modular design, its capacity could be expanded by adding more modules. While it may produce more refined results, training such a huge model may result in increased greenhouse gas emissions if the electricity used is generated from fossil fuels.

Conclusion In this paper, we developed an improved method for the challenging problem of multimodal conditional image synthesis based on IMLE. We addressed the undesirable tradeoff between sample efficiency and sample quality of the prior best IMLE-based method by introducing a novel hierarchical algorithm. We demonstrated on a wide range of tasks that the proposed method achieves the state-of-the-art results in image fidelity without compromising diversity or mode coverage.

Acknowledgements This research was supported by NSERC, WestGrid and the Digital Research Alliance of Canada. We thank Tristan Engst, Yanshu Zhang, Saurabh Mishra, Mehran Aghabozorgi and Shuman Peng for helpful comments and suggestions, and Kuan-Chieh Wang, Devin Guillory, Tianhao Zhang and Jason Lawrence for feedback on an early draft of this paper.

References

- [1] Eirikur Agustsson, Michael Tschannen, Fabian Mentzer, Radu Timofte, and Luc Van Gool. Generative adversarial networks for extreme learned image compression. In *Proceedings of the IEEE International Conference on Computer Vision*, pages 221–231, 2019.
- [2] Eirikur Agustsson, Michael Tschannen, Fabian Mentzer, Radu Timofte, and Luc Van Gool. Extreme learned image compression with gans. In *CVPR Workshops*, volume 1, page 2, 2018.
- [3] Saeed Anwar, Muhammad Tahir, Chongyi Li, A. Mian, F. Khan, and A. W. Muzaffar. Image colorization: A survey and dataset. *ArXiv*, abs/2008.10774, 2020.
- [4] Yuval Bahat and Tomer Michaeli. Explorable decoding of compressed images. *arXiv preprint arXiv:2006.09332*, 2020.
- [5] S. Baker and T. Kanade. Limits on super-resolution and how to break them. *IEEE Transactions on Pattern Analysis and Machine Intelligence*, 24(9):1167–1183, 2002.
- [6] Georgios Batzolis, Jan Stanczuk, Carola-Bibiane Schönlieb, and Christian Etmann. Non-uniform diffusion models. *arXiv preprint arXiv:2207.09786*, 2022.
- [7] Mikolaj Binkowski, Danica J. Sutherland, Michal Arbel, and Arthur Gretton. Demystifying mmd gans. *ArXiv*, abs/1801.01401, 2018.
- [8] Konstantinos Bousmalis, N. Silberman, David Dohan, D. Erhan, and Dilip Krishnan. Unsupervised pixel-level domain adaptation with generative adversarial networks. *2017 IEEE Conference on Computer Vision and Pattern Recognition (CVPR)*, pages 95–104, 2017.
- [9] Andrew Brock, J. Donahue, and K. Simonyan. Large scale gan training for high fidelity natural image synthesis. *ArXiv*, abs/1809.11096, 2019.
- [10] Bingyi Cao, Andre F. de Araújo, and Jack Sim. Unifying deep local and global features for image search. In *ECCV*, 2020.
- [11] Yun Cao, Zhiming Zhou, Weinan Zhang, and Yong Yu. Unsupervised diverse colorization via generative adversarial networks. *ArXiv*, abs/1702.06674, 2017.
- [12] Fabio Maria Carlucci, Paolo Russo, and Barbara Caputo. $(de)^2co$: Deep depth colorization. *IEEE Robotics and Automation Letters*, 3:2386–2393, 2018.
- [13] Qifeng Chen and Vladlen Koltun. Photographic image synthesis with cascaded refinement networks. In *IEEE International Conference on Computer Vision (ICCV)*, volume 1, page 3, 2017.
- [14] Zezhou Cheng, Qingxiong Yang, and Bin Sheng. Deep colorization. *2015 IEEE International Conference on Computer Vision (ICCV)*, pages 415–423, 2015.
- [15] R. Child. Very deep vaes generalize autoregressive models and can outperform them on images. *ArXiv*, abs/2011.10650, 2020.
- [16] Yunjey Choi, Min-Je Choi, Munyoung Kim, Jung-Woo Ha, S. Kim, and J. Choo. Stargan: Unified generative adversarial networks for multi-domain image-to-image translation. *2018 IEEE/CVF Conference on Computer Vision and Pattern Recognition*, pages 8789–8797, 2018.
- [17] Yunjey Choi, Youngjung Uh, Jaejun Yoo, and Jung-Woo Ha. Stargan v2: Diverse image synthesis for multiple domains. *2020 IEEE/CVF Conference on Computer Vision and Pattern Recognition (CVPR)*, pages 8185–8194, 2020.
- [18] Bin Dai, Ziyu Wang, and David Paul Wipf. The usual suspects? reassessing blame for vae posterior collapse. In *ICML*, 2020.
- [19] Tao Dai, Jianrui Cai, Yongbing Zhang, Shu-Tao Xia, and Lei Zhang. Second-order attention network for single image super-resolution. In *Proceedings of the IEEE Conference on Computer Vision and Pattern Recognition*, pages 11065–11074, 2019.

- [20] Duc-Tien Dang-Nguyen, Cecilia Pasquini, Valentina Conotter, and Giulia Boato. Raise: A raw images dataset for digital image forensics. In *Proceedings of the 6th ACM Multimedia Systems Conference*, pages 219–224, 2015.
- [21] Aditya Deshpande, Jiajun Lu, Mao-Chuang Yeh, Min Jin Chong, and David Alexander Forsyth. Learning diverse image colorization. *2017 IEEE Conference on Computer Vision and Pattern Recognition (CVPR)*, pages 2877–2885, 2017.
- [22] J. Donahue, Philipp Krähenbühl, and Trevor Darrell. Adversarial feature learning. *ArXiv*, abs/1605.09782, 2017.
- [23] Chao Dong, Chen Change Loy, Kaiming He, and Xiaoou Tang. Learning a deep convolutional network for image super-resolution. In *European conference on computer vision*, pages 184–199. Springer, 2014.
- [24] Vincent Dumoulin, Ishmael Belghazi, Ben Poole, Alex Lamb, Martín Arjovsky, Olivier Mastropietro, and Aaron C. Courville. Adversarially learned inference. *ArXiv*, abs/1606.00704, 2017.
- [25] Vincent Dumoulin, Ethan Perez, Nathan Schucher, Florian Strub, Harm de Vries, Aaron C. Courville, and Yoshua Bengio. Feature-wise transformations. *Distill*, 2018.
- [26] Ian Goodfellow, Jean Pouget-Abadie, Mehdi Mirza, Bing Xu, David Warde-Farley, Sherjil Ozair, Aaron Courville, and Yoshua Bengio. Generative adversarial nets. In *Advances in neural information processing systems*, pages 2672–2680, 2014.
- [27] Michael U Gutmann, Ritabrata Dutta, Samuel Kaski, and Jukka Corander. Likelihood-free inference via classification. *arXiv preprint arXiv:1407.4981*, 2014.
- [28] Muhammad Haris, Gregory Shakhnarovich, and Norimichi Ukita. Deep back-projection networks for super-resolution. In *Proceedings of the IEEE conference on computer vision and pattern recognition*, pages 1664–1673, 2018.
- [29] Kaiming He, X. Zhang, Shaoqing Ren, and Jian Sun. Deep residual learning for image recognition. *2016 IEEE Conference on Computer Vision and Pattern Recognition (CVPR)*, pages 770–778, 2016.
- [30] Martin Heusel, Hubert Ramsauer, Thomas Unterthiner, Bernhard Nessler, and Sepp Hochreiter. Gans trained by a two time-scale update rule converge to a local nash equilibrium. In *Advances in neural information processing systems*, pages 6626–6637, 2017.
- [31] Jonathan Ho, Ajay Jain, and P. Abbeel. Denoising diffusion probabilistic models. *ArXiv*, abs/2006.11239, 2020.
- [32] Jonathan Ho, Ajay Jain, and Pieter Abbeel. Denoising diffusion probabilistic models. *Advances in Neural Information Processing Systems*, 33:6840–6851, 2020.
- [33] Xueqi Hu, Xinyue Zhou, Qiusheng Huang, Zhengyi Shi, Li Sun, and Qingli Li. Qs-attn: Query-selected attention for contrastive learning in i2i translation. *arXiv preprint arXiv:2203.08483*, 2022.
- [34] X. Huang, Ming-Yu Liu, Serge J. Belongie, and J. Kautz. Multimodal unsupervised image-to-image translation. *ArXiv*, abs/1804.04732, 2018.
- [35] Xun Huang and Serge J. Belongie. Arbitrary style transfer in real-time with adaptive instance normalization. *2017 IEEE International Conference on Computer Vision (ICCV)*, pages 1510–1519, 2017.
- [36] S. Iizuka, Edgar Simo-Serra, and H. Ishikawa. Let there be color! *ACM Transactions on Graphics (TOG)*, 35:1 – 11, 2016.
- [37] Phillip Isola, Jun-Yan Zhu, Tinghui Zhou, and Alexei A Efros. Image-to-image translation with conditional adversarial networks. In *Proceedings of the IEEE conference on computer vision and pattern recognition*, pages 1125–1134, 2017.

- [38] Alexia Jolicoeur-Martineau, Ke Li, Rémi Piché-Taillefer, Tal Kachman, and Ioannis Mitliagkas. Gotta go fast when generating data with score-based models. *arXiv preprint arXiv:2105.14080*, 2021.
- [39] Tero Karras, S. Laine, and Timo Aila. A style-based generator architecture for generative adversarial networks. *2019 IEEE/CVF Conference on Computer Vision and Pattern Recognition (CVPR)*, pages 4396–4405, 2019.
- [40] Tero Karras, S. Laine, Miika Aittala, Janne Hellsten, J. Lehtinen, and Timo Aila. Analyzing and improving the image quality of stylegan. *2020 IEEE/CVF Conference on Computer Vision and Pattern Recognition (CVPR)*, pages 8107–8116, 2020.
- [41] Tero Karras, Samuli Laine, and Timo Aila. A style-based generator architecture for generative adversarial networks. In *Proceedings of the IEEE conference on computer vision and pattern recognition*, pages 4401–4410, 2019.
- [42] Bahjat Kawar, Michael Elad, Stefano Ermon, and Jiaming Song. Denoising diffusion restoration models. In *Advances in Neural Information Processing Systems*, 2022.
- [43] Jiwon Kim, Jung Kwon Lee, and Kyoung Mu Lee. Accurate image super-resolution using very deep convolutional networks. In *Proceedings of the IEEE conference on computer vision and pattern recognition*, pages 1646–1654, 2016.
- [44] Diederik P. Kingma and Jimmy Ba. Adam: A method for stochastic optimization. *CoRR*, abs/1412.6980, 2015.
- [45] Diederik P Kingma and Max Welling. Auto-encoding variational bayes. *arXiv preprint arXiv:1312.6114*, 2013.
- [46] Pierre-Yves Laffont, Zhile Ren, Xiaofeng Tao, Chao Qian, and James Hays. Transient attributes for high-level understanding and editing of outdoor scenes. *ACM Transactions on Graphics (TOG)*, 33:1 – 11, 2014.
- [47] Wei-Sheng Lai, Jia-Bin Huang, Narendra Ahuja, and Ming-Hsuan Yang. Deep laplacian pyramid networks for fast and accurate super-resolution. *2017 IEEE Conference on Computer Vision and Pattern Recognition (CVPR)*, pages 5835–5843, 2017.
- [48] Gustav Larsson, M. Maire, and Gregory Shakhnarovich. Learning representations for automatic colorization. *ArXiv*, abs/1603.06668, 2016.
- [49] Christian Ledig, Lucas Theis, Ferenc Huszár, Jose Caballero, Andrew Cunningham, Alejandro Acosta, Andrew P Aitken, Alykhan Tejani, Johannes Totz, Zehan Wang, et al. Photo-realistic single image super-resolution using a generative adversarial network. In *CVPR*, volume 2, page 4, 2017.
- [50] Hsin-Ying Lee, Hung-Yu Tseng, Jia-Bin Huang, Maneesh Kumar Singh, and Ming-Hsuan Yang. Diverse image-to-image translation via disentangled representations. In *ECCV*, 2018.
- [51] Hsin-Ying Lee, Hung-Yu Tseng, Qi Mao, Jia-Bin Huang, Yu-Ding Lu, Maneesh Kumar Singh, and Ming-Hsuan Yang. Drit++: Diverse image-to-image translation via disentangled representations. *International Journal of Computer Vision*, pages 1–16, 2020.
- [52] Ke Li and Jitendra Malik. Implicit maximum likelihood estimation. *arXiv preprint arXiv:1809.09087*, 2018.
- [53] Ke Li*, Shichong Peng*, Tianhao Zhang*, and Jitendra Malik. Multimodal image synthesis with conditional implicit maximum likelihood estimation. *International Journal of Computer Vision*, May 2020.
- [54] Zhen Li, Jinglei Yang, Zheng Liu, Xiaomin Yang, Gwanggil Jeon, and Wei Wu. Feedback network for image super-resolution. In *Proceedings of the IEEE Conference on Computer Vision and Pattern Recognition*, pages 3867–3876, 2019.
- [55] Ming-Yu Liu, T. Breuel, and J. Kautz. Unsupervised image-to-image translation networks. In *NIPS*, 2017.

- [56] Rui Liu, Yixiao Ge, Ching Lam Choi, Xiaogang Wang, and Hongsheng Li. DivCo : Diverse conditional image synthesis via contrastive generative adversarial network. *2021 IEEE/CVF Conference on Computer Vision and Pattern Recognition (CVPR)*, pages 16372–16381, 2021.
- [57] James Lucas, G. Tucker, Roger B. Grosse, and Mohammad Norouzi. Don’t blame the elbo! a linear vae perspective on posterior collapse. In *NeurIPS*, 2019.
- [58] Zhiming Luo, Akshaya Kumar Mishra, Andrew Achkar, Justin A. Eichel, Shaozi Li, and Pierre-Marc Jodoin. Non-local deep features for salient object detection. *2017 IEEE Conference on Computer Vision and Pattern Recognition (CVPR)*, pages 6593–6601, 2017.
- [59] Xuezhe Ma, Xiang Kong, Shanghang Zhang, and Eduard H. Hovy. Decoupling global and local representations via invertible generative flows. In *ICLR*, 2021.
- [60] Qi Mao, Hsin-Ying Lee, Hung-Yu Tseng, Siwei Ma, and Ming-Hsuan Yang. Mode seeking generative adversarial networks for diverse image synthesis. *2019 IEEE/CVF Conference on Computer Vision and Pattern Recognition (CVPR)*, pages 1429–1437, 2019.
- [61] Luke Metz, Ben Poole, David Pfau, and Jascha Sohl-Dickstein. Unrolled generative adversarial networks. In *ICLR*, 2017.
- [62] Mehdi Mirza and Simon Osindero. Conditional generative adversarial nets. *arXiv preprint arXiv:1411.1784*, 2014.
- [63] Kamal Nasrollahi and Thomas B. Moeslund. Super-resolution: a comprehensive survey. *Machine Vision and Applications*, 25:1423–1468, 2014.
- [64] Augustus Odena, Christopher Olah, and Jonathon Shlens. Conditional image synthesis with auxiliary classifier gans. In *International conference on machine learning*, pages 2642–2651, 2017.
- [65] Yingxue Pang, Jianxin Lin, Tao Qin, and Zhibo Chen. Image-to-image translation: Methods and applications. *ArXiv*, abs/2101.08629, 2021.
- [66] Seong-Jin Park, Hyeongseok Son, Sunghyun Cho, Ki-Sang Hong, and Seungyong Lee. SRfeat: Single image super-resolution with feature discrimination. In *Proceedings of the European Conference on Computer Vision (ECCV)*, pages 439–455, 2018.
- [67] Taesung Park, Alexei A. Efros, Richard Zhang, and Jun-Yan Zhu. Contrastive learning for unpaired image-to-image translation. In *European Conference on Computer Vision*, 2020.
- [68] Alec Radford, Luke Metz, and Soumith Chintala. Unsupervised representation learning with deep convolutional generative adversarial networks. *arXiv preprint arXiv:1511.06434*, 2015.
- [69] Scott Reed, Zeynep Akata, Xinchun Yan, Lajanugen Logeswaran, Bernt Schiele, and Honglak Lee. Generative adversarial text to image synthesis. *arXiv preprint arXiv:1605.05396*, 2016.
- [70] Danilo Jimenez Rezende, Shakir Mohamed, and Daan Wierstra. Stochastic backpropagation and variational inference in deep latent gaussian models. In *International Conference on Machine Learning*, 2014.
- [71] Mehdi S. M. Sajjadi, Olivier Bachem, Mario Lucic, Olivier Bousquet, and Sylvain Gelly. Assessing generative models via precision and recall. In *NeurIPS*, 2018.
- [72] Mehdi S. M. Sajjadi, Bernhard Schölkopf, and Michael Hirsch. Enhancenet: Single image super-resolution through automated texture synthesis. *2017 IEEE International Conference on Computer Vision (ICCV)*, pages 4501–4510, 2017.
- [73] Tim Salimans and Diederik P. Kingma. Weight normalization: A simple reparameterization to accelerate training of deep neural networks. *ArXiv*, abs/1602.07868, 2016.
- [74] Sungyong Seo, Jing Huang, Hao Yang, and Yan Liu. Interpretable convolutional neural networks with dual local and global attention for review rating prediction. *Proceedings of the Eleventh ACM Conference on Recommender Systems*, 2017.

- [75] Tamar Rott Shaham, Michaël Gharbi, Richard Zhang, Eli Shechtman, and Tomer Michaeli. Spatially-adaptive pixelwise networks for fast image translation. *2021 IEEE/CVF Conference on Computer Vision and Pattern Recognition (CVPR)*, pages 14877–14886, 2021.
- [76] Taizhang Shang, Qiuju Dai, Shengchen Zhu, Tong Yang, and Yandong Guo. Perceptual extreme super resolution network with receptive field block. *2020 IEEE/CVF Conference on Computer Vision and Pattern Recognition Workshops (CVPRW)*, pages 1778–1787, 2020.
- [77] Jascha Sohl-Dickstein, Eric Weiss, Niru Maheswaranathan, and Surya Ganguli. Deep unsupervised learning using nonequilibrium thermodynamics. In *International Conference on Machine Learning*, pages 2256–2265. PMLR, 2015.
- [78] Yang Song and S. Ermon. Generative modeling by estimating gradients of the data distribution. *ArXiv*, abs/1907.05600, 2019.
- [79] Jheng-Wei Su, Hung kuo Chu, and Jia-Bin Huang. Instance-aware image colorization. *2020 IEEE/CVF Conference on Computer Vision and Pattern Recognition (CVPR)*, pages 7965–7974, 2020.
- [80] Ying Tai, Jian Yang, and Xiaoming Liu. Image super-resolution via deep recursive residual network. In *Proceedings of the IEEE conference on computer vision and pattern recognition*, pages 3147–3155, 2017.
- [81] Yaniv Taigman, A. Polyak, and Lior Wolf. Unsupervised cross-domain image generation. *ArXiv*, abs/1611.02200, 2017.
- [82] Chunwei Tian, Yong Xu, Lunke Fei, and Ke Yan. Deep learning for image denoising: A survey. *ArXiv*, abs/1810.05052, 2018.
- [83] Arash Vahdat and J. Kautz. Nvae: A deep hierarchical variational autoencoder. *ArXiv*, abs/2007.03898, 2020.
- [84] Lijun Wang, Huchuan Lu, Xiang Ruan, and Ming-Hsuan Yang. Deep networks for saliency detection via local estimation and global search. *2015 IEEE Conference on Computer Vision and Pattern Recognition (CVPR)*, pages 3183–3192, 2015.
- [85] Tianyang Wang, M. Sun, and Kaoning Hu. Dilated residual network for image denoising. *ArXiv*, abs/1708.05473, 2017.
- [86] Ting-Chun Wang, Ming-Yu Liu, Jun-Yan Zhu, Andrew Tao, Jan Kautz, and Bryan Catanzaro. High-resolution image synthesis and semantic manipulation with conditional gans. *2018 IEEE/CVF Conference on Computer Vision and Pattern Recognition*, pages 8798–8807, 2018.
- [87] Xintao Wang, Ke Yu, Shixiang Wu, Jinjin Gu, Yihao Liu, Chao Dong, Chen Change Loy, Yu Qiao, and Xiaoou Tang. Esrgan: Enhanced super-resolution generative adversarial networks. *CoRR*, abs/1809.00219, 2018.
- [88] Yifan Wang, Federico Perazzi, Brian McWilliams, Alexander Sorkine-Hornung, Olga Sorkine-Hornung, and Christopher Schroers. A fully progressive approach to single-image super-resolution. In *Proceedings of the IEEE Conference on Computer Vision and Pattern Recognition Workshops*, pages 864–873, 2018.
- [89] Zhihao Wang, Jian Chen, and Steven CH Hoi. Deep learning for image super-resolution: A survey. *IEEE Transactions on Pattern Analysis and Machine Intelligence*, 2020.
- [90] Xiangyu Xu, Deqing Sun, Jinshan Pan, Yujin Zhang, Hanspeter Pfister, and Ming-Hsuan Yang. Learning to super-resolve blurry face and text images. In *Proceedings of the IEEE international conference on computer vision*, pages 251–260, 2017.
- [91] Chih-Yuan Yang, Chao Ma, and Ming-Hsuan Yang. Single-image super-resolution: A benchmark. In *Proceedings of European Conference on Computer Vision*, 2014.
- [92] Zili Yi, Hao Zhang, P. Tan, and Minglun Gong. Dualgan: Unsupervised dual learning for image-to-image translation. *2017 IEEE International Conference on Computer Vision (ICCV)*, pages 2868–2876, 2017.

- [93] Donggeun Yoo, Namil Kim, S. Park, Anthony S. Paek, and In-So Kweon. Pixel-level domain transfer. *ArXiv*, abs/1603.07442, 2016.
- [94] Yuan Yuan, Siyuan Liu, Jiawei Zhang, Yongbing Zhang, Chao Dong, and Liang Lin. Un-supervised image super-resolution using cycle-in-cycle generative adversarial networks. In *Proceedings of the IEEE Conference on Computer Vision and Pattern Recognition Workshops*, pages 701–710, 2018.
- [95] Fangneng Zhan, Jiahui Zhang, Yingchen Yu, Rongliang Wu, and Shijian Lu. Modulated contrast for versatile image synthesis. In *Proceedings of the IEEE/CVF Conference on Computer Vision and Pattern Recognition*, 2022.
- [96] K. Zhang, Shuhang Gu, Radu Timofte, Taizhang Shang, Qiuju Dai, Shengchen Zhu, Tong Yang, Yandong Guo, Younghyun Jo, Sejong Yang, Seon Joo Kim, Lin Zha, Jiande Jiang, Xinbo Gao, Wen Lu, Jing Liu, Kwangjin Yoon, Taegyun Jeon, Kazutoshi Akita, Takeru Ooba, Norimichi Ukita, Zhipeng Luo, Yuehan Yao, Z. Xu, Dongliang He, Wenhao Wu, Yukang Ding, Chao Li, Fu Li, Shilei Wen, Jianwei Li, Fuzhi Yang, Huan Yang, Jianlong Fu, Byung-Hoon Kim, JaeHyun Baek, J. C. Ye, Yuchen Fan, Thomas S. Huang, Junyeop Lee, Bokyeung Lee, Jungki Min, Gwantaek Kim, Kanghyu Lee, Jaihyun Park, Mykola Mykhailych, Haoyu Zhong, Yukai Shi, Xiaojun Yang, Zhijing Yang, Liang Lin, Tongtong Zhao, Jinjia Peng, Huibing Wang, Zhi Jin, Jiahao Wu, Yifu Chen, Chenming Shang, Huanrong Zhang, Jeongki Min, S HrishikeshP., Densen Puthussery, and V JijiC. Ntire 2020 challenge on perceptual extreme super-resolution: Methods and results. *2020 IEEE/CVF Conference on Computer Vision and Pattern Recognition Workshops (CVPRW)*, pages 2045–2057, 2020.
- [97] K. Zhang, W. Zuo, Yunjin Chen, Deyu Meng, and Lei Zhang. Beyond a gaussian denoiser: Residual learning of deep cnn for image denoising. *IEEE Transactions on Image Processing*, 26:3142–3155, 2017.
- [98] K. Zhang, W. Zuo, and Lei Zhang. Ffdnet: Toward a fast and flexible solution for cnn-based image denoising. *IEEE Transactions on Image Processing*, 27:4608–4622, 2018.
- [99] Kai Zhang, W. Zuo, and Lei Zhang. Learning a single convolutional super-resolution network for multiple degradations. *2018 IEEE/CVF Conference on Computer Vision and Pattern Recognition*, pages 3262–3271, 2018.
- [100] Richard Zhang, Phillip Isola, and Alexei A Efros. Colorful image colorization. In *European Conference on Computer Vision*, pages 649–666. Springer, 2016.
- [101] Richard Zhang, Phillip Isola, Alexei A Efros, Eli Shechtman, and Oliver Wang. The unreasonable effectiveness of deep features as a perceptual metric. In *Proceedings of the IEEE conference on computer vision and pattern recognition*, pages 586–595, 2018.
- [102] Yulun Zhang, Yapeng Tian, Yu Kong, Bineng Zhong, and Yun Fu. Residual dense network for image super-resolution. *CoRR*, abs/1802.08797, 2018.
- [103] Jiaojiao Zhao, J. Han, Ling Shao, and Cees G. M. Snoek. Pixelated semantic colorization. *International Journal of Computer Vision*, 128:818–834, 2019.
- [104] Jun-Yan Zhu, Taesung Park, Phillip Isola, and Alexei A. Efros. Unpaired image-to-image translation using cycle-consistent adversarial networks. *2017 IEEE International Conference on Computer Vision (ICCV)*, pages 2242–2251, 2017.
- [105] Jun-Yan Zhu, Richard Zhang, Deepak Pathak, Trevor Darrell, Alexei A. Efros, O. Wang, and E. Shechtman. Toward multimodal image-to-image translation. In *NIPS*, 2017.

A Implementation Details

Architecture As introduced in Sect. 2.3, we adopt a model architecture that consists of a chain of modules. Each module consists of two streams, a local processing stream and a global processing stream. In terms of the backbone architecture of the two streams, the local processing stream consists of residual-in-residual dense blocks (RRDB) [87] as shown in Figure 8. Unlike traditional RRDB, which comes without normalization and deliberately removes batch normalization in particular, we apply weight normalization [73] to all convolution layers. The global processing stream consists of a sequence of dense layers, known as a mapping network [41]. The outputs from the mapping network apply adaptive instance normalization (AdaIN) [35, 25] to the output produced by each RRDB.

Details of RRDB In Figure 8, we show the inner workings of each RRDB, which contains dense blocks and residual connections.

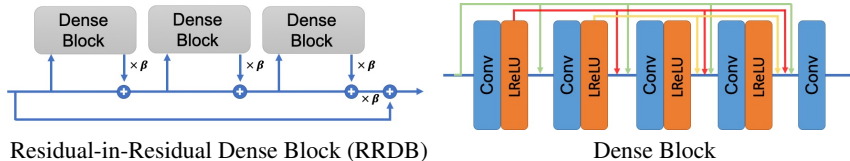
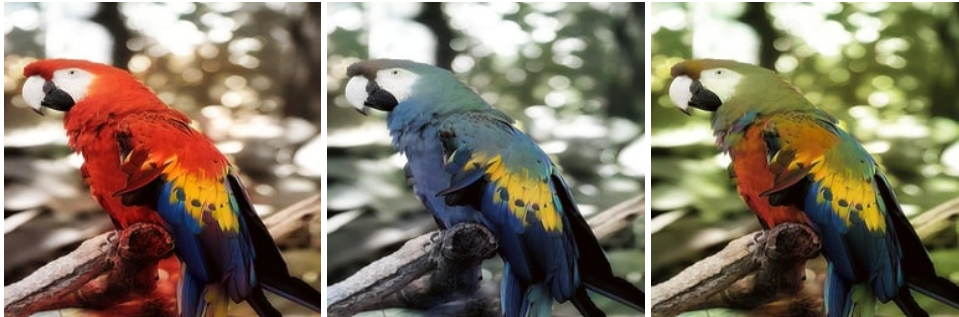


Figure 8: (a) Inner workings of Residual-in-Residual Dense Blocks (RRDBs), which comprises of dense blocks (details in (b)). β is the residual scaling parameter. (b) Inner workings of dense blocks.

Global and Local Stream Effects In Figure 9a we can see that by varying the latent code input to the local stream only, local textures details like the distribution of the colour on the parrot’s wing change while in Figure 9b, by varying the latent code input to the global stream only, global features like the colour tone change.



Varying Latent Code To The Local Stream



Varying Latent Code To The Global Stream

Figure 9: Varying latent code input to (a) the local stream: capturing different local spatial features like the distribution of colour spots on the image. In this example, the wing and the chest of the parrot change from red to blue. (b) the global stream: capturing diverse global features like the colour tone of the image. In this example, the tone changes from red to blue and to green.

B Experiment Details and More Results

We include more details and results on night-to-day, $16\times$ super-resolution, colourization and image decompression in the following pages. For tasks that only show a single sample from the models, we also show different samples for the same input as videos on the project website.

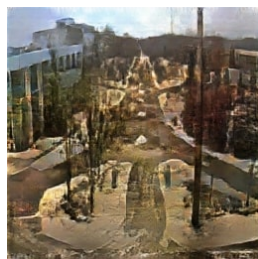
B.1 Night-to-day

We compare our method, CHIMLE, to the best prior IMLE-based method, cIMLE [53], and general-purpose conditional image synthesis methods, BicycleGAN [105], MSGAN [60], DivCo [56], MoNCE [95] and NDM [6] on the Transient Attributes Dataset [46]. As indicated by the quantitative metric in Table 1 and 2, DDRM failed on this task; so we omit the qualitative samples for it.

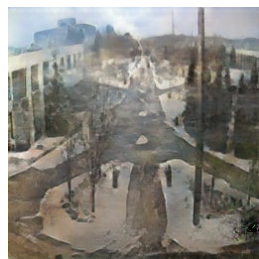




Input



BicycleGAN



MSGAN



DivCo



MoNCE



NDM



cIMLE

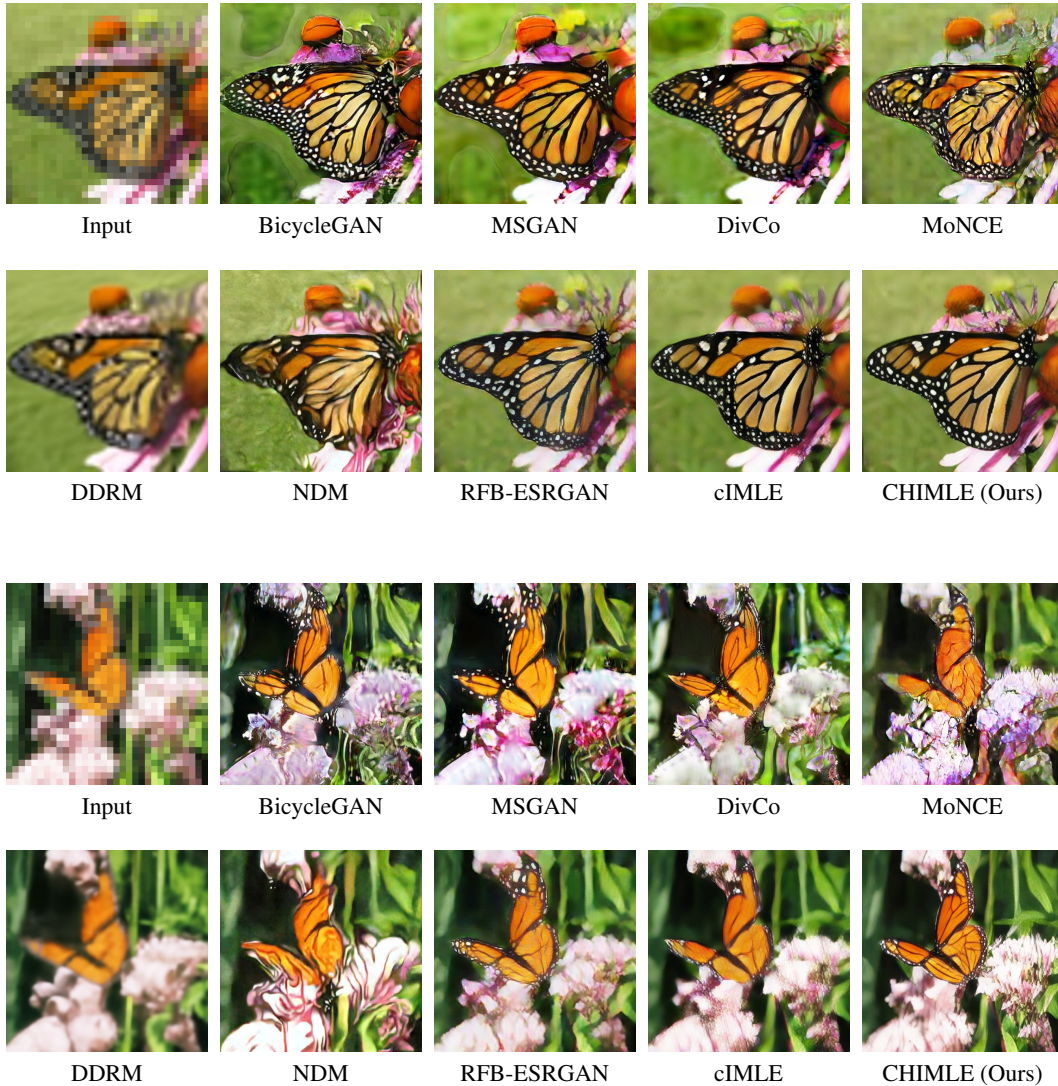


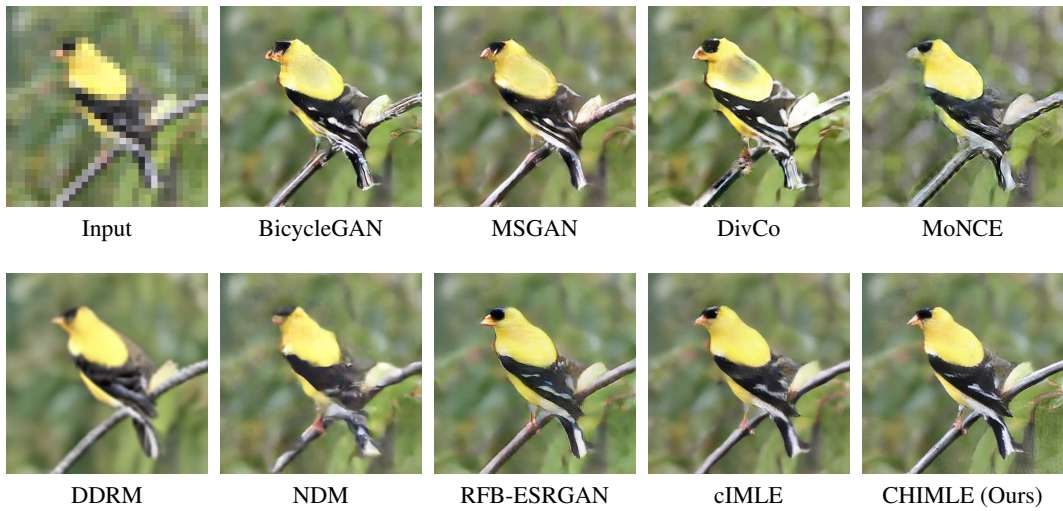
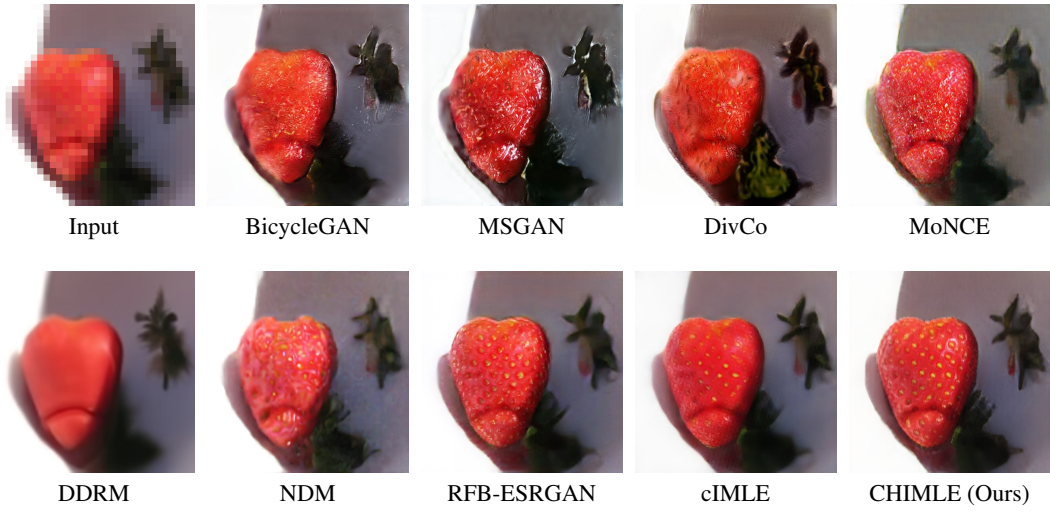
CHIMLE (Ours)

B.2 16× Super-Resolution

Given a low-resolution input image, the goal is to generate different possible higher-resolution output images that are all geometrically consistent with the input. Applications include photo enhancement, remote sensing and medical imaging. We apply our method to the more challenging [5] setting of 16× upscaling, where the input image resolution is 32×32 and the output image resolution is 512×512 .

We select three categories from the ILSVRC-2012 dataset and compare our method, CHIMLE, to the best prior IMLE-based method, cIMLE [53], and general-purpose conditional image synthesis methods, BicycleGAN [105], MSGAN [60], DivCo [56], MoNCE [95], DDRM [42] and NDM [6], and a task-specific method, RFB-ESRGAN [76].

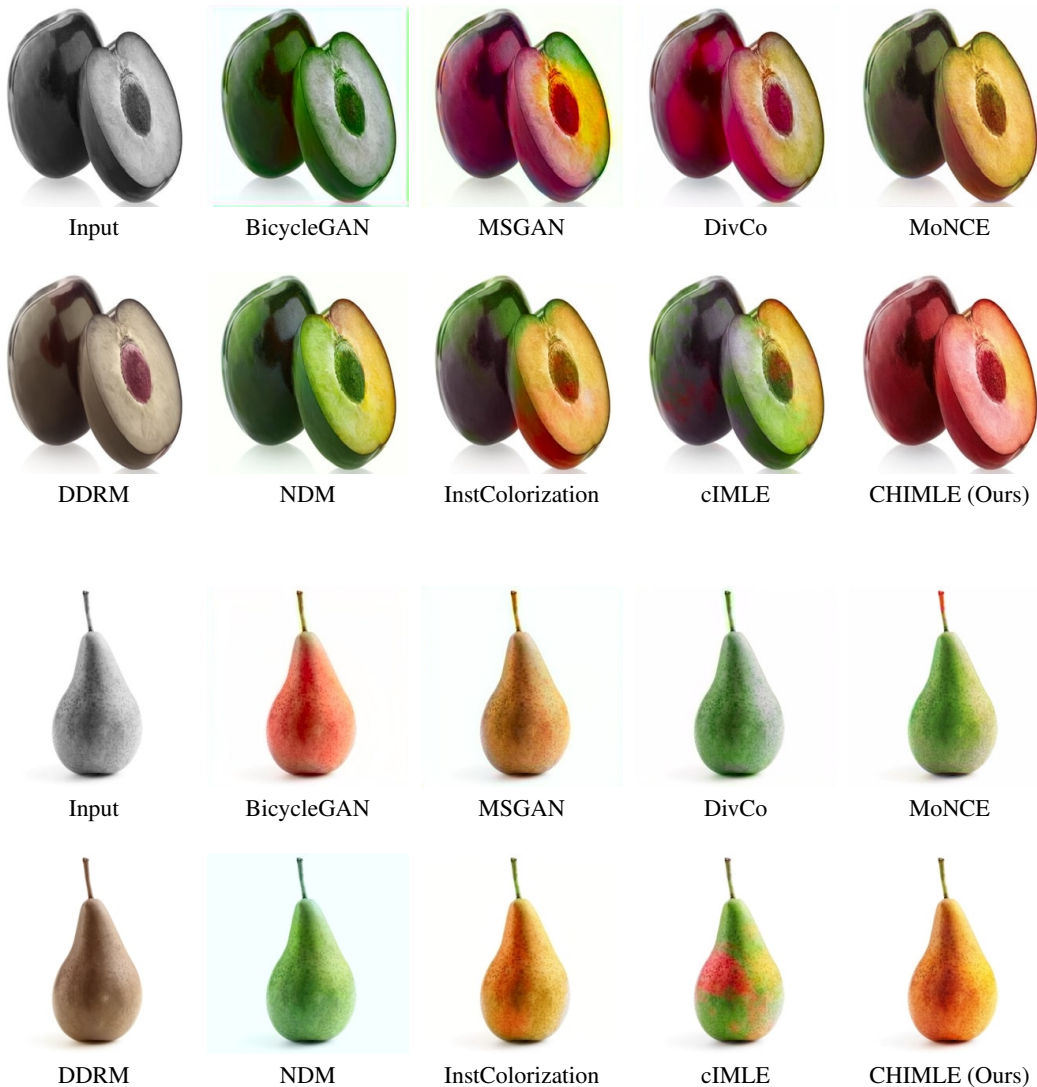


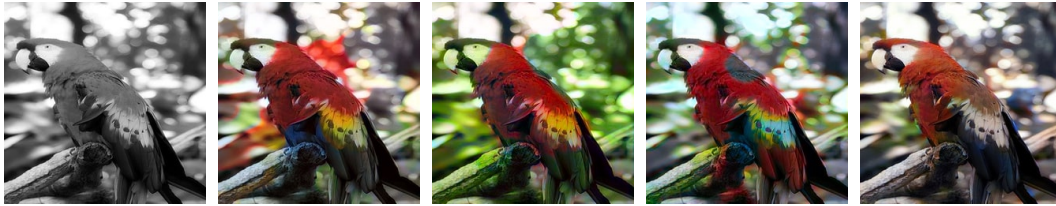


B.3 Image Colourization

Given a grayscale image, the goal is to generate colours for each pixel that are consistent with the content of the input image. Applications include the restoration of old photos, for example those captured by black-and-white cameras or those captured by colour cameras that has become washed out over time. Since there could be many plausible colourings of the same grayscale image, the goal of multimodal colourization is to generate different plausible colourings, which would provide the user the ability to choose the preferred colouring among them.

We compare our method, CHIMLE, to the best prior IMLE-based method, cIMLE [53], and general-purpose conditional image synthesis methods, BicycleGAN [105], MSGAN [60], DivCo [56], MoNCE [95], DDRM [42] and NDM [6], and a task-specific method, InstColorization [79], on a subset of two categories from ILSVRC-2012 and the Natural Color Dataset (NCD) [3].





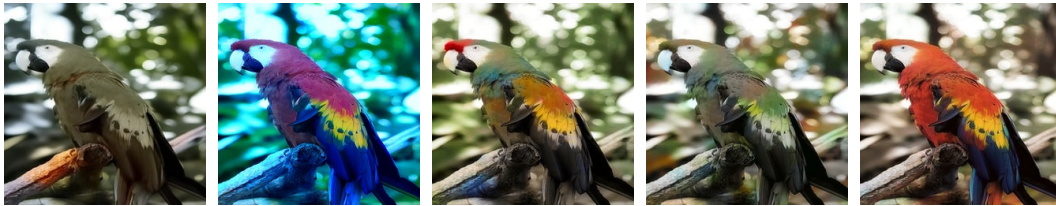
Input

BicycleGAN

MSGAN

DivCo

MoNCE



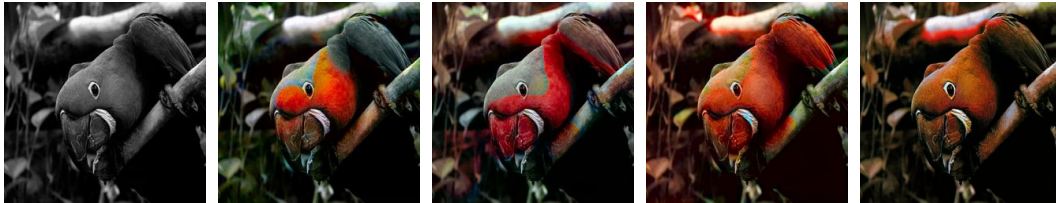
DDRM

NDM

InstColorization

cIMLE

CHIMLE (Ours)



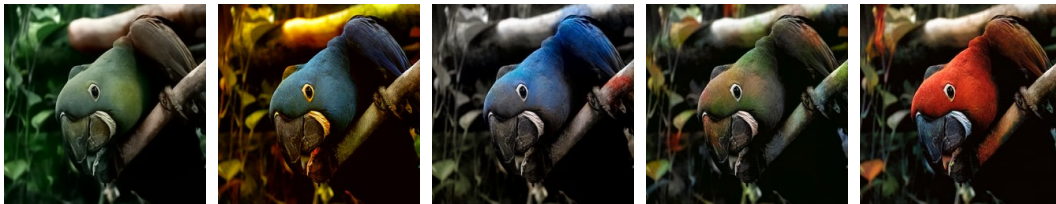
Input

BicycleGAN

MSGAN

DivCo

MoNCE



DDRM

NDM

InstColorization

cIMLE

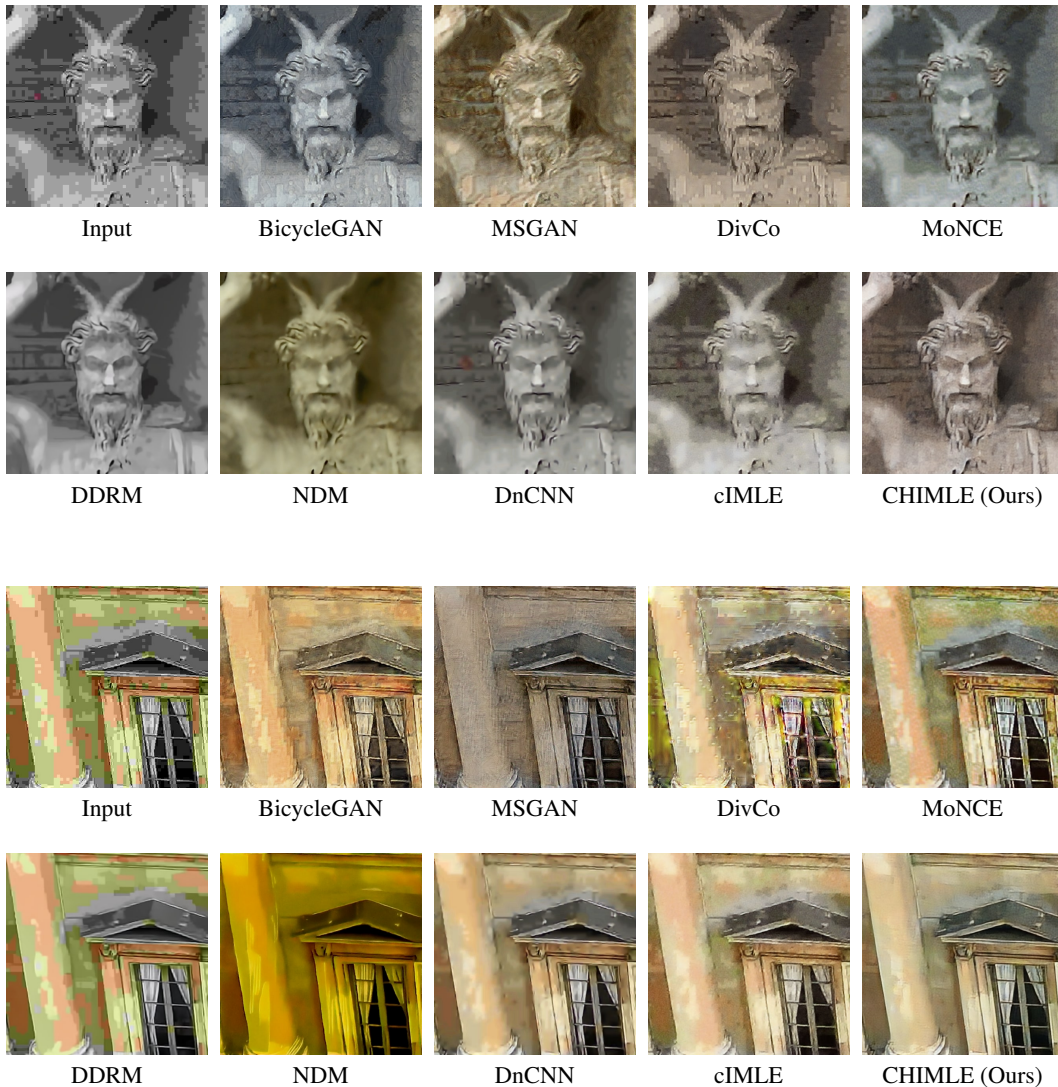
CHIMLE (Ours)

B.4 Image Decompression

Given an image compressed aggressively with a standard lossy codec (e.g.: JPEG), the goal is to recover the original uncompressed image. Note that this task is different from image compression, where both the encoding and decoding model can be learned. Here, the encoding model is fixed (e.g.: JPEG), and only the decoding model is learned.

Image decompression is of practical interest since most images are saved in lossy compressed formats; noticeable artifacts may have been introduced during compression and the original uncompressed images have been lost. It would be nice to have the capability to recover an image free of artifacts. Because compression causes irreversible information loss, multiple artifact-free images are possible. With user guidance, the most preferred version can be selected and saved for future use.

To generate training data, we compressed each image from the RAISE1K [20] dataset using JPEG with a quality of 1%. We compare our method, CHIMLE, to the best prior IMLE-based method, cIMLE [53], and general-purpose conditional image synthesis methods, BicycleGAN [105], MSGAN [60], DivCo [56], MoNCE [95], DDRM [42] and NDM [6], and a task-specific method, DnCNN [97].



C Training Stability

In Figure 10, we visualize the output of CHIMLE for a test input image over the course of training, please refer to the project webpage for the full video. As shown in the video, the output quality improves steadily during training, thereby demonstrating training stability.

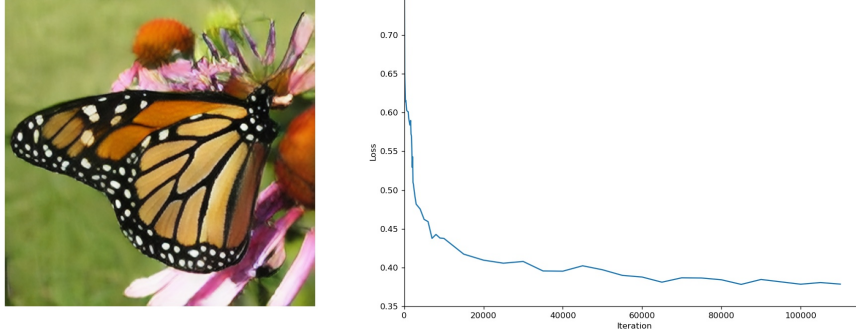


Figure 10: Output of the model at the end of training accompanied by the loss curve over the course of training. See the project webpage for the video showing the output of model while it trains. As shown in the video, the image quality steadily improves and the loss steadily decreases, which shows that training is stable.

D Mode Forcing of Diffusion Models

Consider a discrete-time diffusion model [77, 32]. We denote the data as \mathbf{x}_0 and the latent variables as $\mathbf{x}_{1:T}$. The forward process $q(\mathbf{x}_{1:T}|\mathbf{x}_0)$ is a fixed Markov chain, which satisfies $q(\mathbf{x}_t|\mathbf{x}_{0:t-1}) = q(\mathbf{x}_t|\mathbf{x}_{t-1}) \forall 1 \leq t \leq T$. The reverse process $p_\theta(\mathbf{x}_{0:T})$ is a parameterized Markov chain that we learn, which satisfies $p_\theta(\mathbf{x}_{t-1}|\mathbf{x}_{t:T}) = p_\theta(\mathbf{x}_{t-1}|\mathbf{x}_t) \forall 1 \leq t \leq T$. The likelihood the model assigns to the data is $p_\theta(\mathbf{x}_0) = \int p_\theta(\mathbf{x}_{0:T}) d\mathbf{x}_{1:T}$, which is intractable. So, to train a diffusion model, we cannot maximize likelihood directly and instead maximize the variational lower bound $\mathcal{L}(q, \theta)$, which is a lower bound on the log-likelihood $\log p_\theta(\mathbf{x}_0)$:

$$\mathcal{L}(q, \theta) = \mathbb{E}_{\mathbf{x}_{1:T} \sim q(\mathbf{x}_{1:T}|\mathbf{x}_0)} \left[\log \frac{p_\theta(\mathbf{x}_{0:T})}{q(\mathbf{x}_{1:T}|\mathbf{x}_0)} \right] \quad (3)$$

$$= \mathbb{E}_{\mathbf{x}_{1:T} \sim q(\mathbf{x}_{1:T}|\mathbf{x}_0)} \left[\log \frac{p_\theta(\mathbf{x}_0) p_\theta(\mathbf{x}_{1:T}|\mathbf{x}_0)}{q(\mathbf{x}_{1:T}|\mathbf{x}_0)} \right] \quad (4)$$

$$= \mathbb{E}_{\mathbf{x}_{1:T} \sim q(\mathbf{x}_{1:T}|\mathbf{x}_0)} \left[\log \frac{p_\theta(\mathbf{x}_0) \prod_{t=1}^T p_\theta(\mathbf{x}_t|\mathbf{x}_{0:t-1})}{\prod_{t=1}^T q(\mathbf{x}_t|\mathbf{x}_{0:t-1})} \right] \quad (5)$$

$$= \mathbb{E}_{\mathbf{x}_{1:T} \sim q(\mathbf{x}_{1:T}|\mathbf{x}_0)} \left[\log \frac{p_\theta(\mathbf{x}_0) \prod_{t=1}^T p_\theta(\mathbf{x}_t|\mathbf{x}_{0:t-1})}{\prod_{t=1}^T q(\mathbf{x}_t|\mathbf{x}_{t-1})} \right] \quad (6)$$

$$= \mathbb{E}_{\mathbf{x}_{1:T} \sim q(\mathbf{x}_{1:T}|\mathbf{x}_0)} \left[\log p_\theta(\mathbf{x}_0) + \sum_{t=1}^T \log \frac{p_\theta(\mathbf{x}_t|\mathbf{x}_{0:t-1})}{q(\mathbf{x}_t|\mathbf{x}_{t-1})} \right] \quad (7)$$

$$= \mathbb{E}_{\mathbf{x}_{1:T} \sim q(\mathbf{x}_{1:T}|\mathbf{x}_0)} \left[\log p_\theta(\mathbf{x}_0) - \sum_{t=1}^T \log \frac{q(\mathbf{x}_t|\mathbf{x}_{t-1})}{p_\theta(\mathbf{x}_t|\mathbf{x}_{0:t-1})} \right] \quad (8)$$

$$= \log p_\theta(\mathbf{x}_0) - \sum_{t=1}^T \mathbb{E}_{\mathbf{x}_{1:T} \sim q(\mathbf{x}_{1:T}|\mathbf{x}_0)} \left[\log \frac{q(\mathbf{x}_t|\mathbf{x}_{t-1})}{p_\theta(\mathbf{x}_t|\mathbf{x}_{0:t-1})} \right] \quad (9)$$

Next we will rewrite this in terms of KL divergences. From last page we have:

$$\mathcal{L}(q, \theta) = \log p_\theta(\mathbf{x}_0) - \sum_{t=1}^T \mathbb{E}_{\mathbf{x}_{1:T} \sim q(\mathbf{x}_{1:T} | \mathbf{x}_0)} \left[\log \frac{q(\mathbf{x}_t | \mathbf{x}_{t-1})}{p_\theta(\mathbf{x}_t | \mathbf{x}_{0:t-1})} \right] \quad (10)$$

$$= \log p_\theta(\mathbf{x}_0) - \sum_{t=1}^T \mathbb{E}_{\mathbf{x}_{1:t} \sim q(\mathbf{x}_{1:t} | \mathbf{x}_0)} \left[\log \frac{q(\mathbf{x}_t | \mathbf{x}_{t-1})}{p_\theta(\mathbf{x}_t | \mathbf{x}_{0:t-1})} \right] \quad (11)$$

$$= \log p_\theta(\mathbf{x}_0) - \sum_{t=1}^T \mathbb{E}_{\mathbf{x}_{1:t-1} \sim q(\mathbf{x}_{1:t-1} | \mathbf{x}_0)} \left[\mathbb{E}_{\mathbf{x}_t \sim q(\mathbf{x}_t | \mathbf{x}_{0:t-1})} \left[\log \frac{q(\mathbf{x}_t | \mathbf{x}_{t-1})}{p_\theta(\mathbf{x}_t | \mathbf{x}_{0:t-1})} \right] \right] \quad (12)$$

$$= \log p_\theta(\mathbf{x}_0) - \sum_{t=1}^T \mathbb{E}_{\mathbf{x}_{1:t-1} \sim q(\mathbf{x}_{1:t-1} | \mathbf{x}_0)} \left[\mathbb{E}_{\mathbf{x}_t \sim q(\mathbf{x}_t | \mathbf{x}_{t-1})} \left[\log \frac{q(\mathbf{x}_t | \mathbf{x}_{t-1})}{p_\theta(\mathbf{x}_t | \mathbf{x}_{0:t-1})} \right] \right] \quad (13)$$

$$= \log p_\theta(\mathbf{x}_0) - \sum_{t=1}^T \mathbb{E}_{\mathbf{x}_{1:t-1} \sim q(\mathbf{x}_{1:t-1} | \mathbf{x}_0)} [D_{KL}(q(\mathbf{x}_t | \mathbf{x}_{t-1}) || p_\theta(\mathbf{x}_t | \mathbf{x}_{0:t-1}))] \quad (14)$$

In variational inference, typically we learn both q and θ . Learning q can be seen as finding a variational lower bound $\mathcal{L}(q, \theta)$ that better approximates the log-likelihood $\log p_\theta(\mathbf{x}_0)$, and learning θ can be seen as fitting model parameters according to the variational lower bound. In diffusion models, however, the forward process q is fixed and not learnable.

As a result, whereas typical variational inference can minimize the KL divergences independently of the log-likelihood term by way of choosing q , diffusion models must trade off maximizing log-likelihood against minimizing the KL divergences, because both can only be changed through θ .

Now let's consider the arguments to each KL divergence, namely $q(\mathbf{x}_t | \mathbf{x}_{t-1})$ and $p_\theta(\mathbf{x}_t | \mathbf{x}_{0:t-1})$. The distribution $q(\mathbf{x}_t | \mathbf{x}_{t-1})$ is generally a fixed Gaussian. On the other hand,

$$p_\theta(\mathbf{x}_t | \mathbf{x}_{0:t-1}) \propto p_\theta(\mathbf{x}_t) p_\theta(\mathbf{x}_{0:t-1} | \mathbf{x}_t) \quad (15)$$

$$= p_\theta(\mathbf{x}_t) \prod_{t'=1}^t p_\theta(\mathbf{x}_{t'-1} | \mathbf{x}_{t'}) \quad (16)$$

The distribution $p_\theta(\mathbf{x}_t)$ is the marginal distribution of the sample at step t . The closer t is to 0, the closer $p_\theta(\mathbf{x}_t)$ gets to the likelihood $p_\theta(\mathbf{x}_0)$. Since the distribution of the data can be complex and therefore multimodal, $p_\theta(\mathbf{x}_t)$ can be highly multimodal as well, especially for small t . To arrive at the unnormalized density of $p_\theta(\mathbf{x}_t | \mathbf{x}_{0:t-1})$, we reweight $p_\theta(\mathbf{x}_t)$ according to how likely the reverse process starting from \mathbf{x}_t will follow the path $\mathbf{x}_{1:t-1}$ sampled from the forward process and ultimately get to the data \mathbf{x}_0 . So, as long as there exist multiple modes of $p_\theta(\mathbf{x}_t)$ that can ultimately transition to \mathbf{x}_0 through the reverse process with similar probability (which is expected if the reverse process mixes well), $p_\theta(\mathbf{x}_t | \mathbf{x}_{0:t-1})$ will be multimodal.

Hence, minimizing the KL divergences would make $p_\theta(\mathbf{x}_t)$ similar to $q(\mathbf{x}_t | \mathbf{x}_{t-1})$, which entails making $p_\theta(\mathbf{x}_t)$ unimodal since $q(\mathbf{x}_t | \mathbf{x}_{t-1})$ is a fixed Gaussian. If the variance of $q(\mathbf{x}_t | \mathbf{x}_{t-1})$ along each dimension is greater than that of the modes in the data, this will result in a model that connects the modes together by raising the probability density the model assigns to regions without data. On the other hand, if the variance of $q(\mathbf{x}_t | \mathbf{x}_{t-1})$ along each dimension is smaller than that of the modes in the data, this will result in a model that suppresses some modes in the data by lowering the probability density the model assigns to regions with data. So minimizing the KL divergences can create spurious modes or drop real modes – we call this combined phenomenon *mode forcing* because it forces the creation or removal of modes. Therefore, diffusion models need to strike a balance between maximizing log-likelihood and forcing modes.